Evaluation of the Benefits of Parametric Human Body Model Morphing for Prediction of Injury to Elderly Occupants in Side Impact

Karl-Johan Larsson, Bengt Pipkorn, Johan Iraeus, John H. Bolte IV, Amanda M. Agnew, Jingwen Hu, Matthew P. Reed, Cecilia Sunnevång

Abstract Recently developed Human Body Model (HBM) morphing methods using parametric representative target geometries have enabled morphing of a baseline HBM to many anthropometries, including elderly females. This study investigated the potential benefits for thoracic injury risk prediction of parametric morphing of a HBM. A baseline HBM was morphed to match the subject-specific geometry of two elderly female post mortem human subjects (PMHS) in two steps. First, parametric morphing was performed using target geometries representative of the PMHS's sex, age, stature and mass. In the second step, the parametrically morphed models were further personalized by morphing to subject-specific skeletal geometry and external torso shape. Side-impact sled tests conducted with these PMHS were recreated by means of simulations with the baseline and morphed HBMs. Results showed that the parametrically morphed models showed improved correlation with PMHS kinematics compared with the baseline HBM predictions and performed as well as the further personalized models. Both parametric and personalized HBMs failed to predict the PMHS chestband deflection magnitudes and predicted no risk for rib fractures. In contrast, both PMHS sustained multiple fractured ribs during testing. In conclusion, parametric HBM morphing alone improved prediction of individual kinematics, but neither morphing method improved individual injury risk prediction.

Keywords Elderly, Human Body Model, Morphing, Personalization, Side impact

I. INTRODUCTION

Ageing increases injury and fatality risk for occupants in motor vehicle collisions [1–3], and the number of elderly in the population is increasing [4]. Older females have an increased risk of severe or fatal injury in frontal, rear and side impact collisions compared to other demographic groups [5]. In near-side impact specifically, females see a sharp increase in severe thoracic injury risk with age [6]. Further improvements in side airbag technology could reduce the fatality rates for older occupants [7], but in order to design safety systems that further mitigate fatalities and thoracic injuries, a greater understanding of the injury mechanism is necessary.

Finite element (FE) human body models (HBMs) are a common tool to evaluate injury risk in crash simulations. With recent developments in automated HBM morphing methods using parametric statistical target geometries (Parametric HBMs) [8–10], HBMs can be created that geometrically represent different age, sex, stature and body mass, including HBMs corresponding to elderly females. The Parametric HBM morphing method used in the current work applies a radial basis function (RBF) interpolation between source and target landmarks to modify the shape of a baseline HBM. The source landmarks are selected on the HBM, and parametric statistical target geometries provide the target landmarks. In this study, the parametric geometry models providing the HBM target landmarks describe the ribcage, pelvis, femur, tibia and external body surface geometry. Consequently, the morphed shape of other parts in the Parametric HBM, which are not described by the target geometries, is the result of the RBF interpolation.

Further investigation is needed of the validity and predictive capabilities of a HBM morphed to a new anthropometry. Hwang *et al.* [9] evaluated the correlation of a Total Human Model for Safety version 4.01 (THUMS v4) HBM to test data from two differently sized male post mortem human subjects (PMHS) tested in an unrestrained sled side-impact configuration. The THUMS v4 model was evaluated in its baseline 50th percentile

K. Larsson (e-mail: karl-johan.larsson@chalmers.se; tel: +46 (0)322 626332) is a PhD student in Vehicle Safety and J. Iraeus is a Researcher at Chalmers University of Technology, Gothenburg, Sweden. B. Pipkorn is Adjunct Professor at Chalmers University and Director of Simulation and Active Structures at Autoliv Research, Vårgårda, Sweden, where C. Sunnevång is Vice President Research. J. Bolte IV and A. Agnew are Professor and Associate Professor, respectively, at The Ohio State University, Columbus, OH, USA. J. Hu and M. Reed are Research Associate Professor and D. B. Chaffin Collegiate Research Professor, respectively, at University of Michigan Transportation Research Institute, USA.

male configuration, parametrically morphed using sex, age, stature and body mass of the individual PMHS (Parametric HBMs), and as morphed to subject-specific skeletal geometry extracted from each PMHS's CT data (Personalized HBMs). Correlation to test data for contact forces between HBM body parts and impactor segments were objectively evaluated using CORrelation Analysis (CORA) cross-correlation rating [11]. In addition, accelerations in the spine and peak chestband lateral deflections were compared to PMHS results. The predictions from the Parametric HBMs and the Personalized HBMs were similar, and the predictions from the morphed models were closer to the PMHS test results than the predictions from the baseline HBM.

However, the test condition did not include any restraints, such as seat belt and airbag, and no evaluation of the HBM's capability to predict thoracic injury risk in terms of rib fractures was performed. Predicting the interaction between the occupant, the vehicle and restraints and the resulting thoracic injury risk in a crash is key to the development of safety systems that provide refined protection.

The aim of this study is to investigate the potential benefits in terms of kinematic response and thoracic injury risk prediction on the material level, by means of Parametric HBM morphing in a realistic near-side impact scenario, and to compare the Parametric HBM predictions to Personalized and Baseline HBMs.

II. METHODS

Side-impact sled tests performed with two elderly female PMHS were recreated by means of FE simulations with HBMs. Parametric and Personalized morphed versions of a Baseline HBM were created to represent the PMHS. Sled test simulation results from the Baseline, Parametric and Personalized HBMs were compared to results from the corresponding test.

Fig. 1. The sled test setup from Shurtz *et al.* [12] showing seated PMHS on the sled (test 1701). To the right, the driver door interior is mounted on a 4-zone ASIS system. Between subject and door interior is the unfolded airbag.

Reference PMHS tests Shurtz *et al.* [12] presented near-side impact sled tests with two elderly female PMHS (Table I). The sled test comprised a production seat, retractor pre-tensioning 3-point seatbelt, a dual chamber side-impact airbag, and the driver door interior trim. A dual sled system simulated both lateral acceleration and 4-zone door intrusion with an Advanced Side Impact System (ASIS) (Fig. 1). The PMHS were instrumented with accelerometers on the spine and manubrium, strain gauges on the ribs to identify fracture timing, and dual chestbands on the torso at the level of axilla (armpit) and xiphoid process (lower end of sternum). Prior to impact, the coordinates in the sled environment of landmarks on the seated subjects were recorded. Multiple rib fractures occurred during the sled test for both subjects. From the rib strain gauge data, the timing of thoracic AIS=3 injury severity was identified.

TABLE I
PMHS DATA

Test No.	Sex (M/F)	Age (Years)	Stature (mm)	Mass (kg)	BMI (kg/m^2)	Number of fractured ribs	AIS=3 timing (ms)
1701	F	61	1660	56	20.3	Left: 4, Right: 1	39
1702	F	83	1550	44	18.3	Left: 6, Right: 6	21

Sled test modelling The simulation model of the sled test environment comprised seat, door interior, foam block to capture the head, airbag model and a 3-point seatbelt model with pre-tensioning. The seat with attached airbag model was constrained to a rigid plate representing the sled, and the door interior model was constrained to four rigid plates representing the ASIS (Fig. 2).

During each sled test, airbag pressure from both chambers and accelerations of the sled and the four ASIS zones was recorded. The corresponding measured airbag pressures were prescribed to the airbag model and the recorded sled and ASIS accelerations described the motion of the corresponding parts in the sled model when simulating the respective sled test. The modelling method was validated with matching sled test and simulation performed with a SID-IIs dummy and LS-Dyna dummy model (SID-IIs SBL-D V3.3.2, Humanetics Innovative Solutions, Inc) (Appendix B). All simulations in this study were performed using LS-Dyna MPP Single precision R9.2.0 Revision 119543 (Livermore Software Technology Corporation, Livermore, CA, USA).

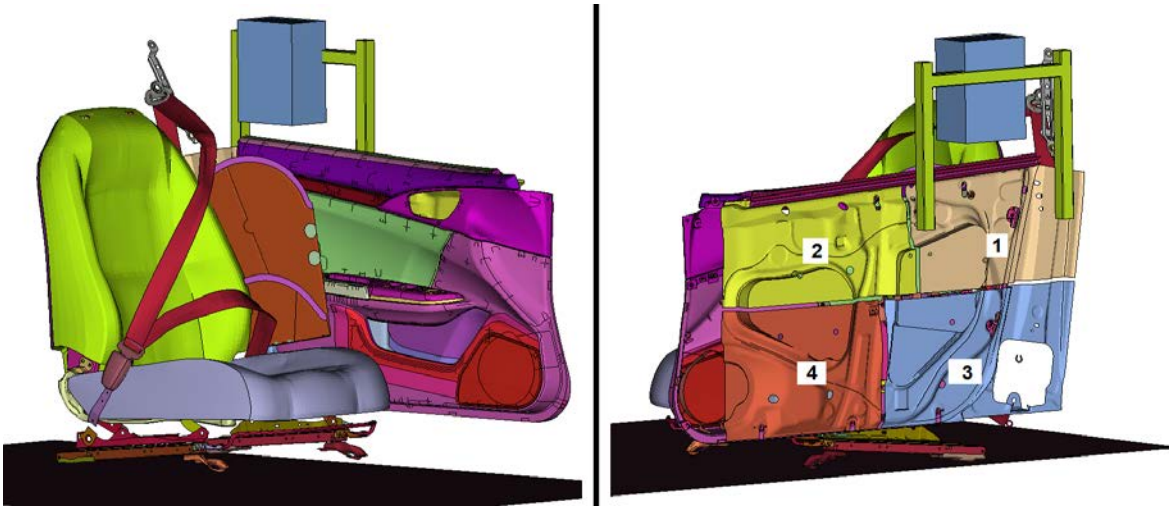

Fig. 2. The sled test simulation model. *Left*: the rigid plate representing the sled (bottom), seat, 3-point seatbelt, airbag, door interior and foam block. *Right*: the four separate rigid plates representing the respective ASIS zones.

Human body modelling The baseline HBM used in this study was SAFER HBM version 9, which is a modified THUMS v3 representing a 50th percentile male. The ribcage model was updated to the geometry of a 50th percentile male ribcage, with generic ribs with varying cortical thickness.

Fig. 3. The 50th percentile male baseline HBM used in this study. The meshes used for tracking external torso contour deformation at axilla and xiphoid level (model chestbands) can be seen on the model torso.

The ribcage model was validated in single rib anterior-posterior bending (force and strain predictions), denuded thorax indentor impacts (force, rib displacement and strain predictions) and in PMHS sled test simulations (rib displacement and strain predictions) [13]. The capability of the SAFER HBM version 9 to predict the risk of two or more fractured ribs was then validated in PMHS table top and sled test simulations, as well as

in accident reconstructions and population based stochastic frontal and near-side impact simulations [14]. Risk of fractured ribs was predicted using a probabilistic strain based criterion [15]. Further modifications from the THUMS v3 are detailed in Appendix A.

For this study, the model was further modified around the axilla region to model arm to torso contact. Originally the flesh of the arms intersected the outer layer of the torso flesh. Since chestband deformation at the axilla level on the external torso surface in lateral impact was of interest in this study, the arm and axilla mesh were locally modified to be intersection-free up to the axilla chestband level. The arm to torso contact was modified to apply contact pressure at the outer layer of the torso flesh. This was important to be able to capture local chestband deformation, which could be generated by the arm being pressed against the torso during door intrusion.

In the HBM, external torso deformation was tracked using two 30 mm-wide bands of shell elements representing chestbands at the axilla and xiphoid level (Fig. 3). These shell elements were tied to the torso surface of the model and had no stiffness, thus neglecting any stiffness contribution of the actual chestbands, which have been found to be negligible for PMHS thoracic deformation in frontal impact [16].

In this study the HBM was evaluated in three configurations in each sled test simulation: as Baseline HBM, as Parametric HBM and as Personalized HBM. The material properties, such as cortical bone stiffness or thickness, were kept constant when morphing, but densities of soft tissue materials (flesh of trunk, neck, arms and legs) were adjusted such that the morphed models had the same total body mass as the corresponding PMHS.

Baseline HBM simulations The Baseline HBM was simulated in both sled tests. Since the Baseline HBM was larger than the two PMHS, PMHS landmark coordinates were not used as positioning targets. Instead, the Baseline HBM was positioned in the sled model using a target driver posture predicted by a driver posture model [17] for a 45-year-old male, 175 cm tall with weight of 75 kg. The fore-aft position of the seat model was not changed from the test position. The deformed seat cushion surfaces were stored after positioning simulations for all HBMs such that an initial contact pressure between HBM and seat could be applied in the sled test simulation by the LS-Dyna *INITIAL_FOAM_REFERENCE_GEOMETRY keyword.

Parametric HBM simulations The Baseline HBM was morphed using the parametric HBM morphing methodology [10], based on the sex, age, stature and body mass index (BMI) of each test subject, resulting in Parametric HBMs.

After morphing, the densities of the soft tissues in the HBM trunk, legs, arms and neck were uniformly scaled so that HBM mass matched the target subject mass. Furthermore, all discrete muscle elements in the HBM (*MAT_SPRING_MUSCLE in LS-Dyna) had their initial length parameter reset to the length obtained after morphing. The model chestbands were reapplied as straight bands at the axilla and xiphoid level on the Parametric HBMs. The HBM internal contact definitions were inspected for intersections and, if present, they were removed by small nodal movement.

The Parametric HBMs were positioned in the sled model in a pre-simulation using the recorded locations of the respective PMHS landmarks as positioning targets. Target locations included head (nose and ears), left and right acromion, elbows, wrists, greater trochanters of the femora, knees and ankles.

Personalized HBM simulations The Parametric HBMs were the starting point for the Personalized HBMs. The 3D geometries of the ribcage, scapula, clavicle and humerus were segmented from supine pre-test clinical resolution CT scans of each subject using 3D-Slicer v4.8.1 [18] (segment editor module, threshold for bone 100+ Hounsfield units). For the ribs and the sternum, homologous landmarks for morphing were selected on both the HBM and the subject ribcage 3D geometry according to the method described by Wang *et al*. [19]. This process was only performed for the left side (impacted side) ribs. The ribs were assumed symmetric between left and right side: the morphing landmarks for the left side ribs were reflected to the right side. The HBM ribcage and surrounding elements were morphed using the same RBF interpolation function as the Parametric HBMs.

The shoulder (clavicle, scapula and humerus) was morphed to subject-specific geometry because there were no statistical target geometries specific to these bones in the parametric morphing method. In the PMHS sled tests both subjects were struck in the shoulder and the individual shoulder geometry could therefore have influenced the individual impact kinematics.

The external torso shape of the Parametric HBMs was morphed to fit the respective PMHS calculated chestband contours at axilla and xiphoid level. Methods used to morph shoulders and torso in Personalized HBMs are detailed in Appendix C.

HBM internal contacts were inspected for intersections and, if present, were removed. Discrete muscle element initial length parameters were reset, and finally the mass of the personalized models was adjusted in the same way as for the parametric models.

The Personalized HBMs were then positioned in the sled test model during a pre-simulation using the same recorded PMHS target locations as the Parametric HBMs.

HBM correlation evaluation In order to evaluate model correlations, model output was compared to measured test data from the respective subjects. The compared data comprised velocities integrated from recorded PMHS accelerations, chest deflections calculated from chestband contours and strain gauge measurements from the ribs. Furthermore, a comparison of the predicted risk of rib fractures to the number of fractured ribs was performed.

Lateral accelerations measured in tests at manubrium, T1, T4, T12 and sacrum were integrated to velocities, since the accelerometer data exhibited several peak values and were therefore not suitable for the CORA cross-correlation evaluation [11]. CORA cross-correlation rating of model predicted lateral velocities at the corresponding HBM locations was performed. For the Baseline HBM the CORA rating was also performed for scaled HBM accelerations integrated to velocities. The scaling method was the equal-stress equal-velocity method (see e.g. [20]) using the respective PMHS mass as reference.

Chestband deformation was tracked at the centre row of nodes from the model chestbands relative to a coordinate system moving with the respective chestband. The origins of these coordinate systems were fixed at the spine location of the model chestband, local y-axis pointing from spine to sternum and local x-axis pointing from HBM left to right. HBM chestband contours were plotted with calculated chestband contours from the corresponding test, by first aligning the respective spine locations and thereafter aligning the spine-sternum direction to the vertical plot axis.

Two chest deflections were calculated from the plotted contours at the corresponding locations along the circumference where the PMHS chestbands showed the largest deformation: Anterior-Posterior (A/P) chest deflection and Lateral chest deflection. A/P deflection was measured as the change in perpendicular distance to a line defined from leftmost to rightmost point on the respective chestband contour. Lateral deflection was quantified by the perpendicular distance of the lateral portion of the chestband to a line defined between the spine and sternum locations on the chestbands. The deflection measurements were normalized by initial distance to the respective line. HBM chest deflections was compared to test data using CORA cross-correlation rating.

Furthermore, rib element strain (element local x-axis strain at the outer element surface, the element local x-axes are directed along the rib) was extracted from the model rib cortical bone at the approximate corresponding location where the subjects had strain gauges mounted on the ribs. The elements chosen to represent the strain gauges were selected from the Personalized HBMs, and the same elements in the Parametric and Baseline HBM ribs were used to extract strain.

A probabilistic method was used to predict the risk of N (N = 1, 2, 3) or more fractured ribs [15]. Instead of employing element deletion to model rib fractures, rib fracture risk was evaluated in a post-processing stage. The maximum first principal strain from each rib cortical bone mesh (24 peak strain values) was selected and an age-adjusted rib fracture risk was calculated from these 24 strain values.

III. RESULTS

Human body modelling

The HBMs as positioned in the sled model are shown for test 1701 (Fig. 4) and for test 1702 (Fig. 5). Morphed model masses were 62.8 kg and 58.3 kg for Parametric and Personalized HBMs respectively before scaling soft tissue densities to reach the target weight of 56 kg in test 1701. In 1702, with occupant mass of 44 kg, the masses were 51.4 kg and 52.2 kg for Parametric and Personalized HBMs respectively before density scaling.

The left-side ribs for Baseline, Parametric and Personalized HBMs overlaid with the segmented subject ribcage for test 1701 are shown in Fig. 6 and for test 1702 in Fig. 7. Chestband profiles for the positioned models at time zero are shown, together with the chestband profiles for the respective PMHS for test 1701 in Fig. 8 and for test 1702 in Fig. 9.

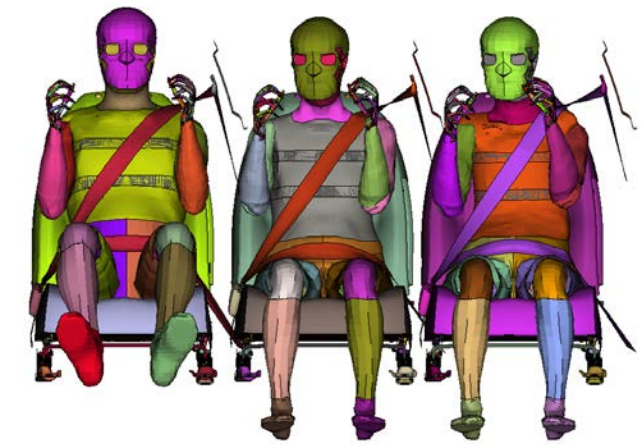

Fig. 4. The positioned HBMs simulated in test 1701. *Left*: Baseline HBM. *Middle*: Parametric HBM. *Right*: Personalized HBM.

Fig. 5. The positioned HBMs simulated in test 1702. *Left*: Baseline HBM. *Middle*: Parametric HBM. *Right*: Personalized HBM.

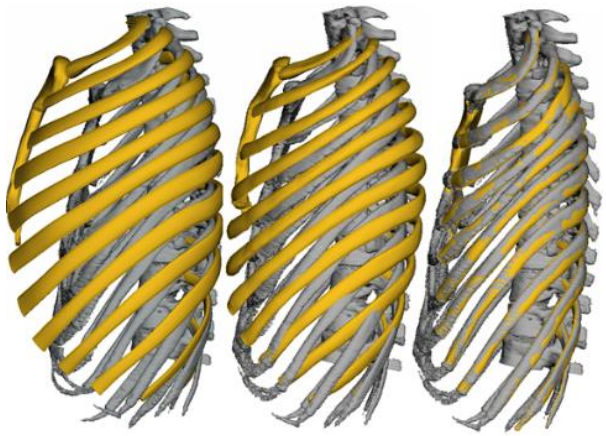

Fig. 6. Subject ribcage (gray) and HBM left-side ribs (yellow) in test 1701. *Left*: Baseline HBM. *Middle*: Parametric HBM. *Right*: Personalized HBM.

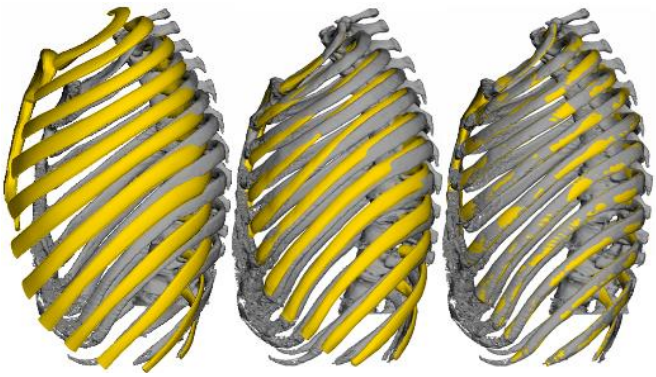

Fig. 7. Subject ribcage (gray) and HBM left-side ribs (yellow) in test 1702. *Left*: Baseline HBM. *Middle*: Parametric HBM. *Right*: Personalized HBM.

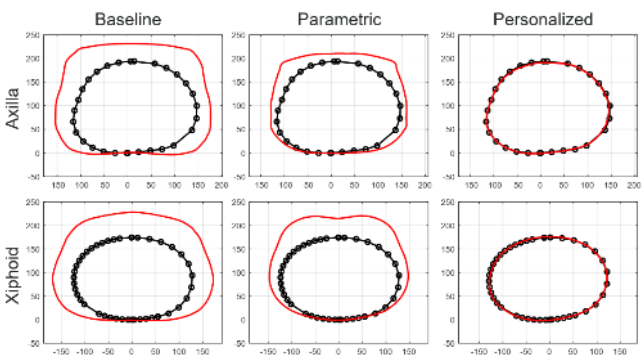

Fig. 8. Chestband profiles at time zero for test 1701 simulations and test. Red curves are HBM, black curves are from PMHS chestband.

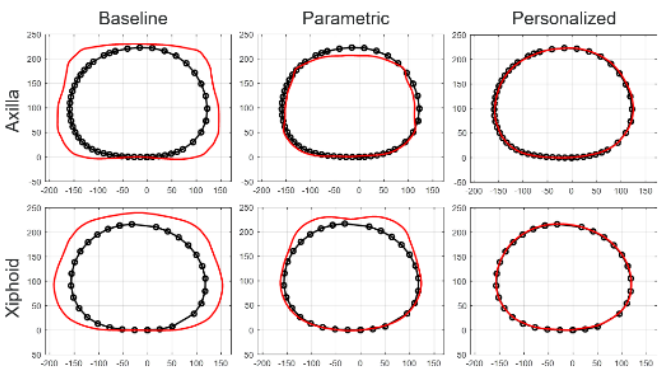

Fig. 9. Chestband profiles at time zero for test 1702 simulations and test. Red curves are the HBM, black curves are from PMHS chestband.

Model correlations evaluation The average CORA cross-correlation ratings for predicted occupant lateral velocities were 0.83, 0.88 and 0.85 for Baseline, Parametric and Personalized HBMs respectively in the test 1701 simulations. For test 1702 simulations the corresponding ratings were 0.76, 0.83 and 0.87 (Table II). Baseline

scaled obtained an average rating of 0.81 in 1701 and 0.76 in 1702. A rating of 1 would indicate a perfect match between test and simulation.

TABLE II
HBMs VS TEST CORA CROSS-CORRELATION RATINGS FOR LATERAL VELOCITIES

Test No.	HBM	Manubrium	T1	T4	T12	Sacrum	Average
1701	Baseline	0.92	0.87	0.88	0.78	0.72	0.83
	Baseline (scaled)	0.81	0.72	0.83	0.84	0.87	0.81
	Parametric	0.97	0.92	0.80	0.73	0.96	0.88
	Personalized	0.85	0.91	0.87	0.77	0.85	0.85
1702	Baseline	0.62	0.70	0.70	0.87	0.89	0.76
	Baseline (scaled)	0.78	0.75	0.69	0.84	0.74	0.76
	Parametric	0.87	0.78	0.73	0.79	0.97	0.83
	Personalized	0.89	0.86	0.80	0.84	0.94	0.87

The chestband contours from HBMs and test 1701 used for calculating A/P and Lateral deflections are plotted in Fig. 10 at the thoracic AIS=3 timing (39 ms) in test 1701. See Appendix D for chestband contours from both tests plotted at 20 ms, 30 ms and 40 ms.

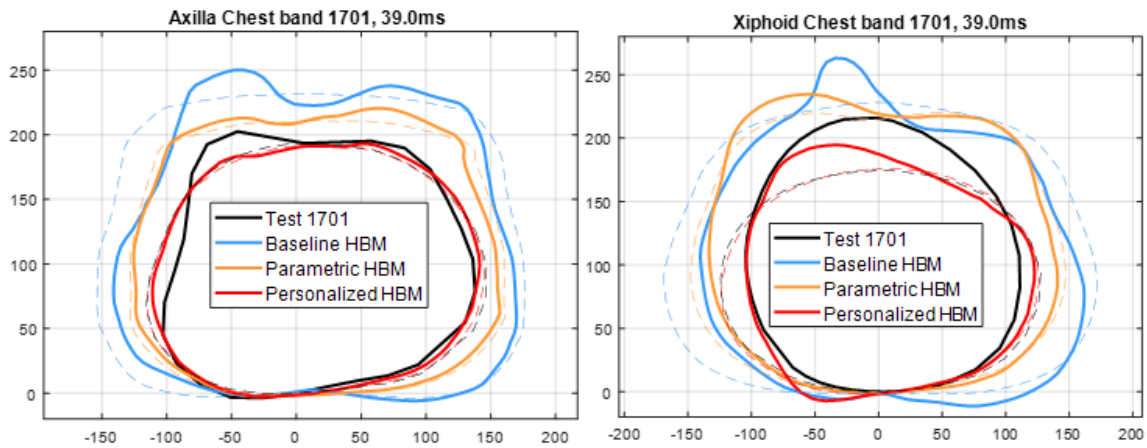

Fig. 10. Axilla (*left*) and Xiphoid (*right*) level chestband contours at thoracic AIS=3 timing in test 1701. Dimensions in mm. Test (black), Baseline HBM (blue), Parametric HBM (orange) and Personalized HBM (red). Dashed lines are corresponding initial contours.

Normalized (to initial half-depth/-width) A/P and Lateral chest deflection histories are plotted in Fig. 11 for test 1701. Compared to the test data, the Parametric and Personalized HBMs show smaller deflections both in A/P and Lateral directions at the Axilla level. At the Xiphoid level the test data show A/P expansion which is smaller in all HBMs. For Xiphoid Lateral deflection, the Baseline and Personalized HBMs predicted a larger deflection than was obtained in the test.

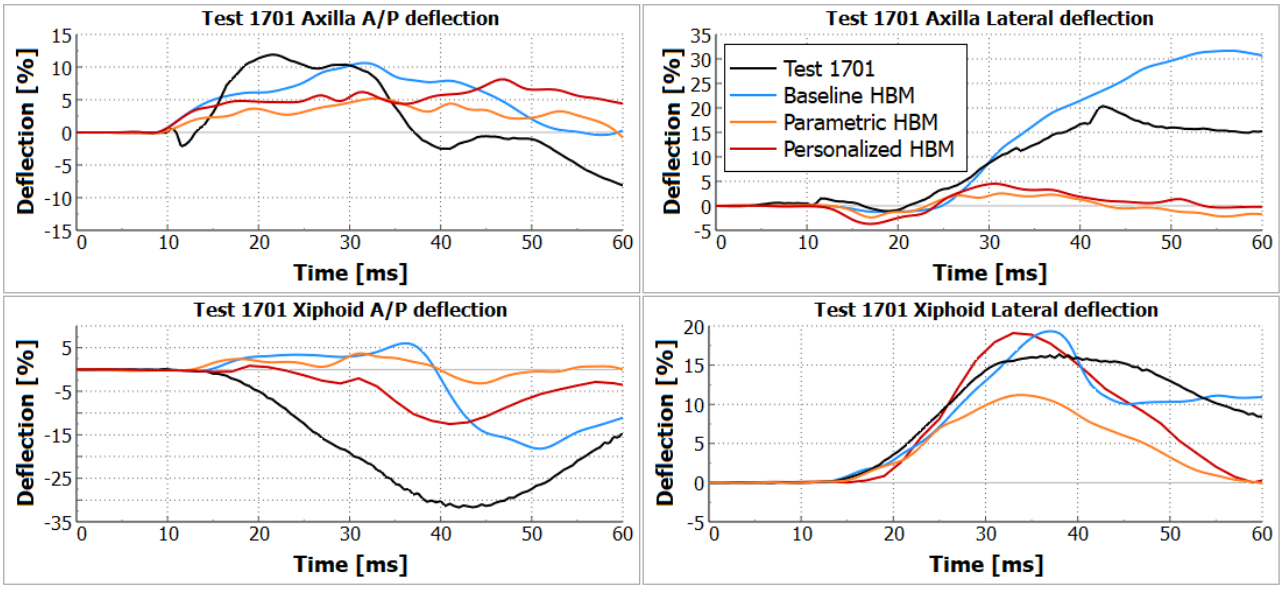

Fig. 11. Test 1701 (black) and HBM-predicted chestband deflections. Negative values correspond to expansion. Baseline HBM (blue), Parametric HBM (orange) and Personalized HBM (red). Top row is Axilla level chest band, bottom row is Xiphoid level chest band. Left column is A/P normalized half-depth deflection. Right column is normalized half-width deflection.

For test 1702 the A/P and Lateral chest deflection histories are plotted in Fig. 12. The Parametric and Personalized HBMs underestimated the deflection magnitudes obtained in the test. The Baseline HBM predicted similar magnitudes for the chest deflections but had a delayed onset of the deflections compared to the test data.

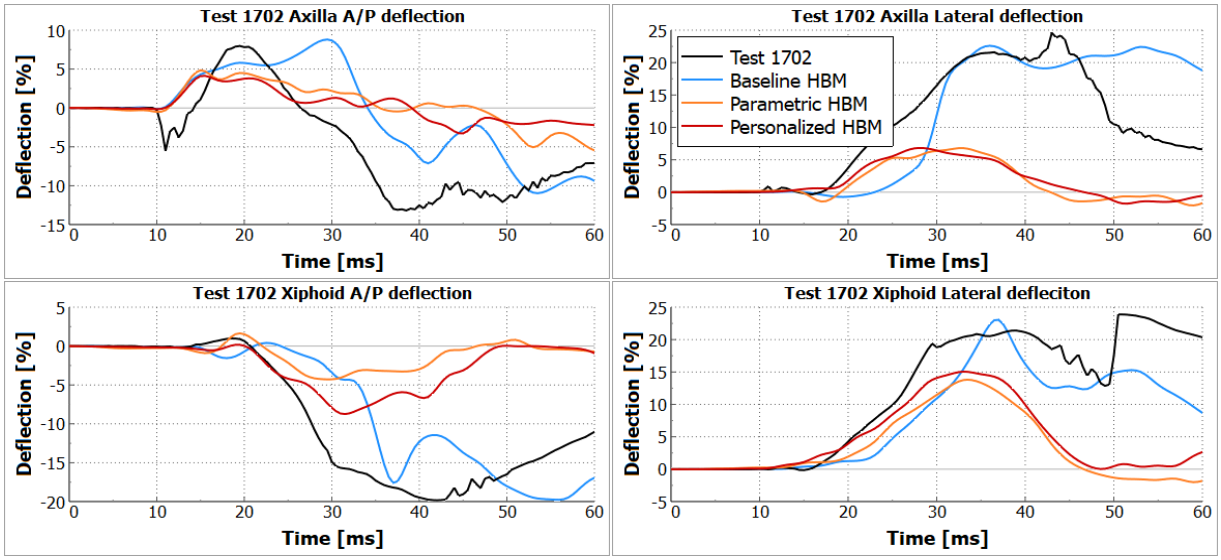

Fig. 12. Test 1702 (black) and HBM-predicted chestband deflections. Negative values correspond to expansion. Baseline HBM (blue), Parametric HBM (orange) and Personalized HBM (red). Top row is Axilla level chest band, Bottom row is Xiphoid level chest band. Left column is A/P normalized half-depth deflection. Right column is normalized half-width deflection.

CORA cross-correlation ratings for chest deflections are presented in Table III. In both tests the Baseline HBM obtained the highest CORA ratings, with an average of 0.57 in test 1701 and 0.61 in 1702. Parametric and Personalized obtained average ratings of 0.23 and 0.45 in test 1701 and 0.32 and 0.41 in test 1702, respectively. Axilla A/P deflection ratings were consistently low for all models in both tests.

TABLE III
HBM VS TEST CORA CROSS-CORRELATION RATINGS FOR CHEST DEFLECTION

Test No.	Chestband	Deflection	Baseline	Parametric	Personalized
1701	Axilla	A/P	0.45	0.22	0.23
		Lateral	0.73	0.12	0.15
	Xiphoid	A/P	0.20	0.00	0.60
		Lateral	0.91	0.56	0.83
		Average 1701	0.57	0.23	0.45
1702	Axilla	A/P	0.30	0.26	0.31
		Lateral	0.77	0.25	0.38
	Xiphoid	A/P	0.64	0.17	0.34
		Lateral	0.72	0.58	0.62
		Average 1702	0.61	0.32	0.41

Rib strain from test and simulation of test 1701, ribs L5 and L6 (see Appendix E for all left-side rib strains) are shown in Fig. 13. For both ribs, onset of posterior strain is delayed compared to test in all HBMs. The Baseline HBM overestimates the compressive strain measured laterally for rib L5, and for rib L6 all HBMs overestimate the compressive lateral strain.

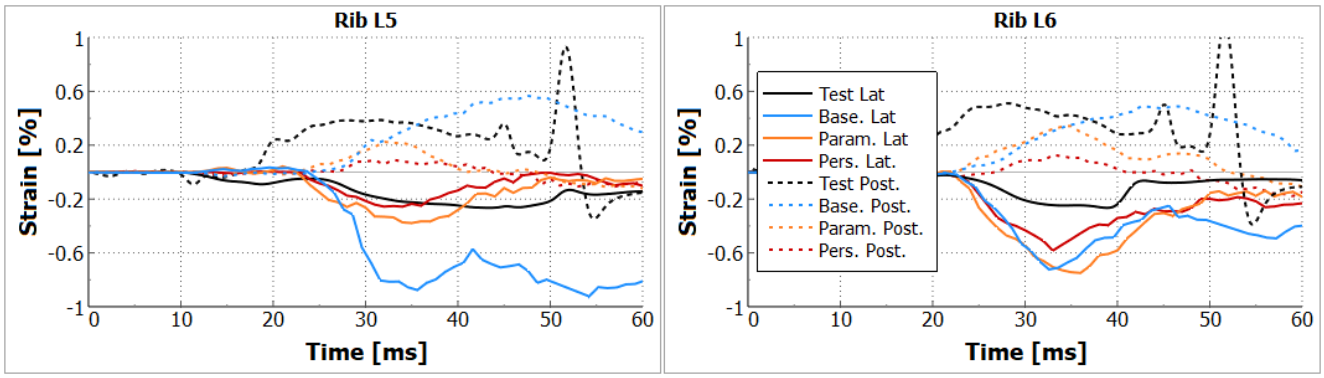

Fig. 13. Rib strain from ribs L5 and L6 from test 1701 and simulations. Solid curves are lateral strain gauges, dashed curves are from posterior strain gauges. Test (black), Baseline HBM (blue), Parametric HBM (orange) and Personalized HBM (red).

For test 1702, rib strain from anterior strain gauges on ribs L2 and L3 are shown in Fig. 14 (see Appendix E for all left-side strain measurements from test 1702). The test data show initial tensile strain on both ribs that is changed into compressive strain after 20 ms. Both Parametric and Personalized HBMs follow the initial rise in tensile strain but drops the tension after a few milliseconds, and then fails to exhibit the compressive strain seen in the test. The Baseline HBM instead showed initial compressive strain, and after 30 ms shows an increase in compressive strain.

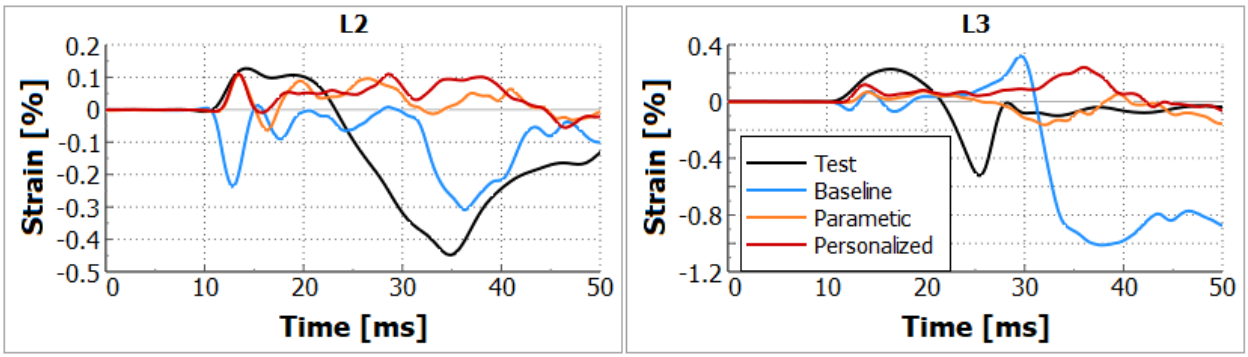

Fig. 14. Test 1702 anterior strain from ribs L2 and L3. Test (black), Baseline HBM (blue), Parametric HBM (orange) and Personalized HBM (red).

For rib fracture risk prediction, the rib maximum first principal strain from the 24-rib cortical bone shell element meshes was extracted. In test 1701 simulations, the Baseline HBM predicted the overall largest strains, with a maximum of 2.0% in rib L4 (Fig. 15). Parametric and Personalized models had overall maximums of 0.7% in ribs L7 and L2, respectively. The Baseline model obtained the highest principal strain values also in the test 1702 simulations (Fig. 16). The largest principal strain values were 1.9%, 1.0% and 0.8% for Baseline, Parametric and Personalized HBMs, respectively.

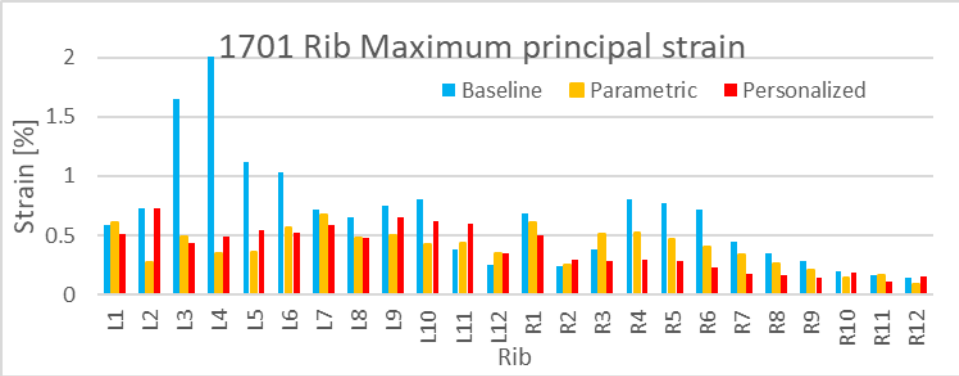

Fig. 15. Test 1701 maximum first principal strains extracted from Baseline (blue), Parametric (orange) and Personalized (red) HBMs.

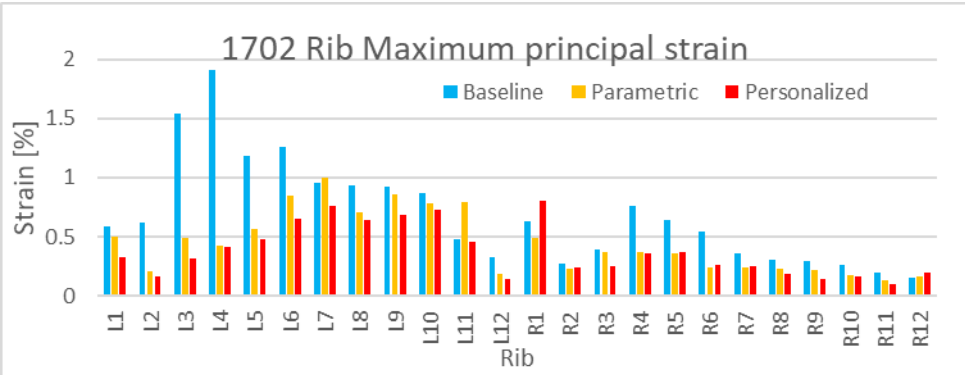

Fig. 16. Test 1702 maximum first principal strains extracted from Baseline (blue), Parametric (orange) and Personalized (red) HBMs.

The age-adjusted risks of fractured ribs (Table IV) were low for all HBMs compared to the number of actual fractured ribs (five in test 1701 and 12 in test 1702). In both tests, Parametric and Personalized HBMs predicted 0% risk of one or more ribs fractured. The Baseline HBM predicted 51% risk for one or more fractured ribs in test 1701 and 63% risk in test 1702.

TABLE IV

PREDICTED RISK OF N OR MORE RIBS FRACTURED, N=1,2,3

Test No.	Age (Years)	HBM	1+	2+	3+
		Baseline	51%	7%	0%
1701	61	Parametric	0%	0%	0%
		Personalized	0%	0%	0%
		Baseline	63%	18%	2%
1702	83	Parametric	0%	0%	0%
		Personalized	0%	0%	0%

IV. DISCUSSION

The Parametric morphing of the Baseline HBM resulted in an overestimation of body mass of 6.8 kg (12% of subject mass) for test 1701 and 7.4 kg (17%) for test 1702. After Personalization morphing mass overestimation was reduced to 2.3 kg (4%) in test 1701 and increased to 8.2 kg (19%) in test 1702. The average density of the

Baseline HBM flesh tissues used for adjusting the morphed model masses was approximately 1,250 kg/m^3, which was high compared to human muscle and fat tissue densities, which are approximately 1,000 kg/m^3. This high density was most likely introduced to compensate for voids in the Baseline HBM resulting from the modelling simplifications done for FE modelling of the human body with limited resolution. The morphing and density scaling of the HBM likely shifted the relative location of the centre of mass for different body segments and the complete HBM, but the effect of this was not considered in this study. Future work should consider the accuracy of mass distribution in the HBM after morphing.

In the Personalization morphing, a small number of solid elements in soft tissues surrounding the ribs in the intercostal muscle mesh and in the torso flesh mesh became inverted in both cases. These elements were adjusted with small nodal movements respecting the shape of the ribs and the torso skin, if possible, or they were deleted if this was not possible. The deletion of these soft tissue elements was judged not to have any significant influence on the studied model response.

By morphing the Baseline HBM, the element shape and thus different element quality measures were affected throughout the model. It was judged that this shape change of the elements would not introduce numerical errors arising from degraded element quality (similar element quality as in the Baseline model). Future work will study suitable element quality criteria for a morphed model.

The positioning of all HBMs in this study was done by pulling the HBMs to specified target locations using constant force cable elements. For the morphed models, positioning to the subject landmarks locations was made such that the relative distance of HBM rib cage to airbag and intruding structure would be as close as possible to the test conditions. By positioning to target locations, gravity equilibrium was not enforced in the models. Considering that a free-falling body would displace less than 2 mm in the 20 ms it took before the intruding structure started pushing the subjects out of the seat, and that all HBMs had some initial contact pressure with the seat model, gravity imbalance was assumed negligible.

As in the previous study by Hwang *et al.* [9], both the Parametric and Personalized HBMs improved correlation with PMHS kinematic data, as judged by the average CORA rating for lateral velocity during the impact, although the benefit was small in the 1701 test condition. Likewise, both Parametric and Personalized models obtained similar CORA ratings in both tests.

For chest deflections, all models in general failed to predict the PMHS results. All HBMs received CORA ratings for chest deflection which would correspond to Unacceptable to Fair biofidelity (0-0.65) on the ISO/TR 9790 [21] biofidelity rating sliding scale, and no HBM obtained an average rating for chest deflection that would correspond to Good biofidelity (rating >0.65).

The processed PMHS chestband test results made several sudden jumps during the events, visible as jumps in the calculated deflections, e.g. Axilla A/P at 10 ms in Fig. 12. These jumps were likely caused by signal noise in the test data and add some uncertainty to the true magnitude of the PMHS chest deflections. However, for most of the duration the test chestband results exhibited a smooth deformation. The HBM chestbands had no stiffness and were constrained to follow the deformation of the external torso surface, which meant that the HBM chestbands could deform also out of the plane where deformation was tracked. The out-of-plane deformations of model chestbands were disregarded when calculating the HBM chest deflections. The physical chestbands used in the tests consist of a padded, thin steel band mounted to the test subjects with a small tension (approx. 40 N) and were assumed to have very small out of plane deformations. The physical chestbands could have separated from the PMHS torso surface during deformation, and such separation could not be captured by the HBM chestbands. The mass of the used chestbands in the tests was approximately 0.4 kg per chestband, and this mass was included in the subject mass that the morphed models were matched to. A possible enhancement for HBM simulation to PMHS test chestband comparison is to model the physical chestbands in future work.

The Baseline HBM showed the largest magnitude normalized chestband deflections, and this should be attributed to the facts that this model had the widest chest, and thus was closer to the intruding structure, and had a larger inertia due to its larger mass. The Personalized and Parametric HBMs in general underpredicted the magnitude of chest deflections obtained in the PMHS tests, except for Xiphoid chestband Lateral deflection for Personalized HBM in test 1701 (Fig. 11).

Peak A/P deflection at the axilla level occurred close to 20 ms in both tests and the HBMs underestimated this deflection. The applied shoulder-belt force magnitudes were similar to the test forces at this time in all simulations (Appendix F). Since the PMHS, in addition to seatbelt pretension, were subjected to lateral loading

from the airbag and door being accelerated by the ASIS, it is possible that the level of intrusion was not correctly captured in the sled modelling.

To investigate the influence of the prescribed ASIS accelerations, additional simulations with the Personalized HBMs were performed where the prescribed acceleration for ASIS zone 1 (the zone closest to occupant torso, Fig. 2) was scaled up by 10%. Comparison of the chestband deflection obtained with this scaled boundary condition to the nominal simulation (Fig. 17, blue and red curves) showed that the larger ASIS acceleration influenced the obtained chestband deflections at both chestbands after about 30 ms, but did not influence the initial chestband deflections. Another possible reason for the underprediction of chestband deflection magnitude in the Parametric and Personalized HBMs was that the models were too stiff to capture the local chest deflections due to the external load sources. To investigate this, the torso flesh material modelling was changed from the THUMS v3 original materials (viscoelastic "flesh" with elastic skin) to a modified version of the neck flesh materials implemented by Östh *et al.* [22] for a detailed female head neck model, which had a softer viscoelastic response (modification and quantification of relative stiffness in Appendix G). With the softer torso flesh model, the chest deflection magnitude increased in A/P and Lateral direction for both chestband levels compared to using the original THUMS v3 flesh modelling (Fig. 17, orange and red curves), indicating that the torso soft tissue modelling had a large influence on the chestband predictions and should be investigated in future work to improve model biofidelity.

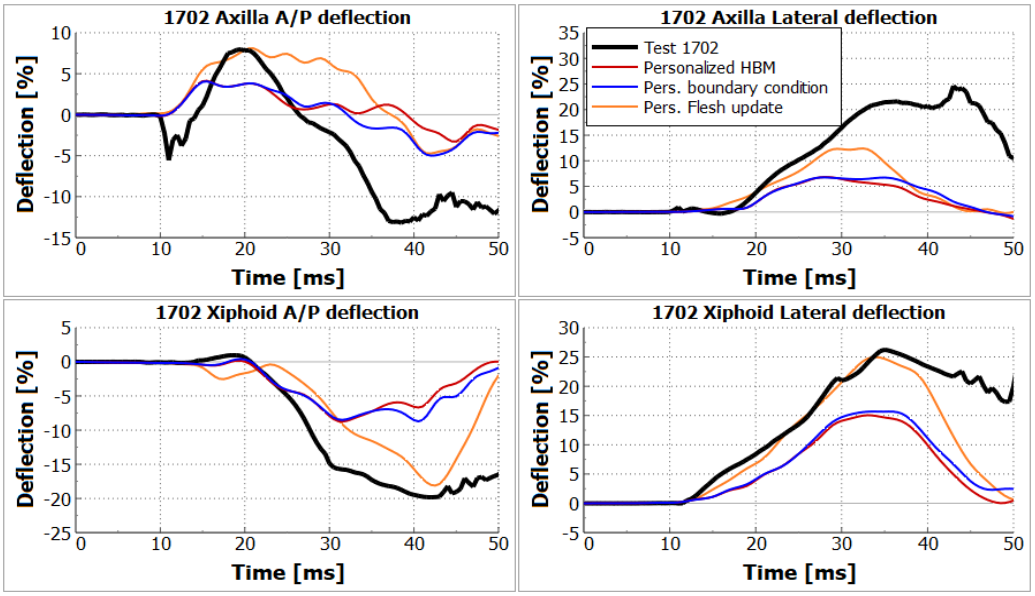

Fig. 17. Test 1702 (black) and 1702 Personalized HBM-predicted chestband deflections during three simulations. Personalized HBM in nominal simulation (red), Personalized HBM with ASIS 1 acceleration scaled up by 10% (blue), Personalized HBM with updated torso flesh modelling (orange).

Due to the large sensitivity of viscoelastic flesh model to chest deflection magnitude in the Personalized HBMs, the force-deflection response in lateral loading of the Baseline HBM was compared to male PMHS test data from a 2.5 m/s, 23 kg oblique lateral pendulum impact [23]. The impact velocity was comparable to the chest band deflection rates in the PMHS test in this study (2-3 m/s).

The Baseline HBM force-deflection response was inside the PMHS corridor up until approximately 20 mm deflection and outside the corridor from 20 to 40 mm deflection (Fig. 18) indicating a slightly stiffer deformation response. Since the morphed models kept the material and cortical thickness properties of the Baseline HBM (except density), it is plausible that they too would be stiff in chest deflection compared to similar females. This will be investigated in future work.

Several other factors than torso flesh material model may influence model chest deflection in the HBMs, such as the arm contact (arm soft tissue geometry and material model), the ribcage model and the modelling of internal organs inside the ribcage.

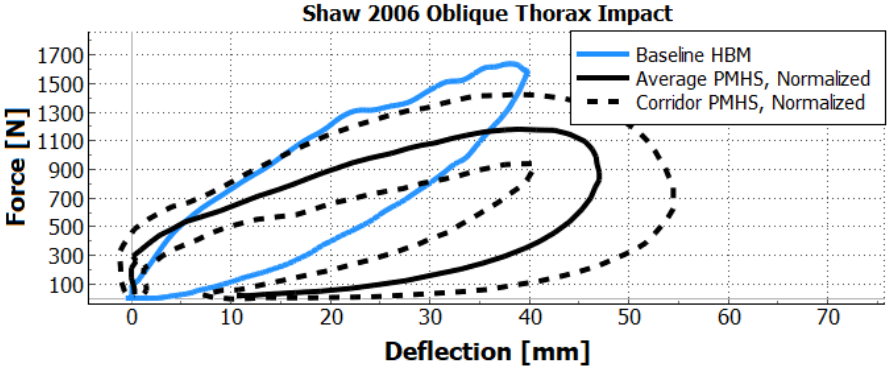

Fig. 18. Thoracic force-deflection response from oblique 2.5m/s pendulum impacts. 50th percentile male PMHS average response (solid black), PMHS response corridor (dashed black) and Baseline HBM (blue).

A limitation in this study, that also could have influenced the results was the airbag modelling. In this study the measured airbag pressures from the corresponding test was prescribed to the airbag model. The benefit of using the measured pressures from the tests was that all HBMs were subjected the same dynamic airbag pressures as the corresponding PMHS during the impact. This airbag modelling underpredicted the pressures the Baseline HBM simulations would have generated if the inflator to airbag mass-flow and airbag ventilation was modelled, since the larger mass of the Baseline HBM would further constrain the expansion of the airbag than the smaller PMHS masses. However, deviations from the test results would then also depend on the obtained airbag pressures in addition to the Baseline HBM response. Therefore, the test pressures were used in all simulations.

No CORA rating of rib strain histories was performed, since predicting the chest deflection was considered a prerequisite for predicting the strain in the ribs.

The comparison of predicted rib strain to gauge data in test 1701 (Fig. 13 and Appendix E) showed that the Parametric and Personalized HBMs predicted similar or higher values of compressive strains in the lateral aspect of the ribs, indicating that at the local measurement site the HBM rib cortical bone saw higher loadings than the ribs in the test.

These locally higher strains did not translate to a high fracture risk prediction, since the maximum principal strains in the ribcage were 0.7% for both Parametric and Personalized HBMs. In test 1702 the Parametric and Personalized HBMs obtained 1.0% and 0.8% strain, respectively. For comparison, Kemper *et al.* [24] reported an average ultimate strain of 2.2% for rib cortical bone from three female subjects aged 46–64 years old. The Baseline HBM obtained strains close to these levels in a few ribs and consequently was the only HBM to predict any risk of rib fractures.

The probabilistic method used to calculate the risk of fracturing N or more ribs [15] is based on the ultimate strain from tensile coupon testing of rib cortical bone from 12 individuals (Kemper *et al.* [24,25]) aged 18–81 years (average 55 years). The age adjustment performed assumes that the rib ultimate strain is linearly reduced by a factor of 5.1% per decade of aging. The ages of the PMHS in this study were in the upper range and outside of the range of subjects for which coupon testing was carried out. The capability of the current version of the probabilistic rib fracture prediction method and the age adjustment method to predict rib fracture risk for elderly females needs to be investigated.

Rib cortical bone thickness was kept from the baseline male HBM in all simulations and ranged from 0.2 mm to 1.7 mm. For comparison, Schoell *et. al* [26] developed a 65yo HBM and implemented a rib cortical bone thickness of 0.32–1.96 mm, determined from analysis of 222 thoracic CT-scans. This was an indication that the rib cortical bone thickness in the HBMs used in this study is not too thick for the elderly PMHS modelled, based on current literature. The rib material properties were also kept from the male Baseline HBM, an approach also chosen by Davis *et al.* [27] when developing a small female HBM.

However, PMHS individual ribcage mechanical properties might need to be considered in future work to improve fracture risk prediction. Effects such as costal cartilage calcification or rib cortical bone porosity might, on the individual level, influence rib fracture risk. For example, the range of porosity in the rib cortical bone was found to be 7–42% of the cortical bone area for a set of five females aged 77–94 years [28], indicating that individual variations can be large. An increase of porosity in cortical bone has been shown to degrade ultimate

stress in tensile tests on femur cortical bone samples, where female samples exhibited increasing porosity with increasing age [29]. It is also plausible that the modelling of rib cortical bone with relatively coarse shell elements (1–3 mm edge lengths in the Baseline HBM), which assumes a state of plane stress, is insufficient to capture the true state of stress in rib cortical bone loaded in side impact.

The results of this study suggest that only geometric morphing of a HBM to a representative anthropometry, both as Parametric HBM and CT-based Personalized HBM, of an individual elderly female subject does not improve the prediction of thoracic injury risk in side impact of that subject. To improve injury risk prediction in side impact for elderly females by Parametric HBM simulations, individual aspects of the material properties and structural variations (e.g. material thickness distribution, local deficiencies) of soft tissues, ribs and costal cartilage should be quantified and implemented in the HBMs in future work.

V. CONCLUSIONS

Parametric morphing of a HBM to a specific individual anthropometry improved prediction of individual kinematics in side impact. Parametric HBMs performed as well as Personalized HBMs in terms of CORA rating for kinematic prediction, both showing improved predictions compared to the Baseline HBM.

Parametric morphing of a Human Body Model to a specific elderly female individual did not improve prediction of the individual thoracic injury risk in side impact.

VI. ACKNOWLEDGEMENTS

The work performed in this study was funded by FFI-Strategic Vehicle Research and Innovation, by Vinnova, the Swedish Energy Agency, the Swedish Transport Administration and the Swedish vehicle industry. The work was carried out at SAFER – Vehicle and Traffic Safety Centre at Chalmers, Sweden. The authors thank Craig Markusic at Honda R&D Americas, Inc for providing the simulation model of the sled test environment. The authors also thank faculty, staff and students at the Injury Biomechanics Research Center at The Ohio State University for their contributions to this project, especially Yun-Seok Kang, Ben Shurtz, Gretchen Baker, Yadetsie Zaragoza-Rivera, David Stark, Arrianna Willis and Rakshit Ramachandra.

VII. REFERENCES

[1] Kahane, C. J. (2013) Injury Vulnerability and Effectiveness of Occupant Protection Technologies for Older Occupants and Women. Report No. DOT HS 811 766, National Highway Traffic Safety Administration, Washington, D.C

[2] Ridella, S. A., Rupp, J. D., Poland, K. (2012) Age-Related Differences in AIS 3+ Crash Injury Risk, Types, Causation and Mechanisms. *Proceedings of IRCOBI Conference*, 2012, Dublin, Ireland.

[3] Carter, P. M., Flannagan, C. A. C., Reed, M. P., Cunningham, R. M., Rupp, J. D. (2014) Comparing the effects of age, BMI and gender on severe injury (AIS 3+) in motor-vehicle crashes. *Accident Analysis and Prevention*, **72**: pp. 146–60.

[4] He, W., Goodkind, D., Kowal, P. (2016) An Aging World: 2015. *International Population Reports, U.S Census Bureau*.

[5] Hill, J. D., Boyle, L. N. (2006) Assessing the relative risk of severe injury in automotive crashes for older female occupants. *Accident Analysis and Prevention*, **38**(1): pp. 148–54.

[6] Ramachandra, R., Kashikar, T., Bolte IV, J. H. (2017) Injury Patterns of Elderly Occupants Involved in Side Crashes. *Proceedings of IRCOBI Conference*, 2017, Malaga, Spain.

[7] Sunnevang, C., Rosén, E., Bostrom, O. (2009) Real-Life Fatal Outcome in Car-to-Car Near-Side Impacts—Implications for Improved Protection Considering Age and Crash Severity. *Traffic Injury Prevention*, **10**(2): pp. 194–203.

[8] Hwang, E., *et al*. (2016) Rapid Development of Diverse Human Body Models for Crash Simulations through Mesh Morphing. *SAE Technical Paper* 2016-01-1491; doi 10.4271/2016-01-1491.

[9] Hwang, E., *et al*. (2016) Development, Evaluation, and Sensitivity Analysis of Parametric Finite Element Whole-Body Human Models in Side Impacts. *Stapp Car Crash Journal*, **60**(November): pp. 473–508.

[10] Zhang, K., *et al*. (2017) An automated method to morph finite element whole-body human models with a wide range of stature and body shape for both men and women. *Journal of Biomechanics*, **60**: pp. 253–60.

[11] Gehre, C., Gades, H., Wernicke, P. (2009) Objective Rating of Signals Using Test and Simulation Responses. *Enhanced Safety Vehicle (ESV)*, 2009, Paper Number: 09–0407..

[12] Shurtz, B. K., Agnew, A. M., Kang, Y-S, Bolte IV, J. H. (2018) Application of Scaled Deflection Injury Criteria to Two Small, Fragile Females in Side Impact Motor Vehicle Crashes. *SAE Technical Paper* 2018-01-0542:1–8.

[13] Iraeus, J., Pipkorn, B. (2019) Development and Validation of a Generic Finite Element Rib Cage to be used for Strain Based Fracture Prediction. Submitted to *Proceedings of IRCOBI Conference*, 2019, Florence, Italy.

[14] Pipkorn, B., Iraeus, J., Björklund, M., Bunketorp, O., Jakobsson, L. (2019) Multiscale Validation of a Rib Fracture Prediction Method for Human Body Models. Submitted to *Proceedings of IRCOBI Conference*, 2019, Florence, Italy.

[15] Forman, J. L., *et al*. (2012) Predicting rib fracture risk with whole-body finite element models: development and preliminary evaluation of a probabilistic analytical framework. *56th AAAM Annual Conference. Annals of Advances in Automotive Medicine* **56**: pp. 109–24.

[16] Shurtz, B. K., Agnew, A. M., Kang, Y-S, Bolte IV, J. H. (2017) Effect of Chestbands on the Global and Local Response of the Human Thorax to Frontal Impact. *Annals of Biomedical Engineering*, **45**(11): pp. 2663–72.

[17] Park, J., Ebert, S. M., Reed, M. P., Hallman, J. J. (2016) Statistical Models for Predicting Automobile Driving Postures for Men and Women Including Effects of Age. *Human Factors*, **58**(2): pp. 261–78.

[18] Fedorov, A., *et al*. (2012) 3D Slicer as an Image Computing Platform for the Quantitative Imaging Network. *Magnetic Resonance Imaging*, **30**(9): pp. 1323–41.

[19] Wang, Y., *et al*. A parametric ribcage geometry model accounting for variations among the adult population. *Journal of Biomechanics*, **49**(13): pp. 2791–8.

[20] Yoganandan, N., Aru,n M. W. J., Pintar, F. A. (2014) Normalizing and scaling of data to derive human response corridors from impact tests. *Journal of Biomechanics*, **47**(8): pp.1749–56.

[21] International Organization for Standardization. (1999) Technical Report 9790; Road Vehicles; Anthropomorphic Side Impact Dummy - Lateral Impact Response Requirements to Assess the Biofidelity of the Dummy. Geneva, 1999.

[22] Östh, J., *et al*. (2017) A female head–neck model for rear impact simulations. *Journal of Biomechanics*, **51**: pp. 49–56.

[23] Shaw, J. M., Herriott, R. G., McFadden, J. D., Donnelly, B. R., Bolte, J. H. (2006) Oblique and Lateral Impact Response of the PMHS Thorax. *Stapp Car Crash Journal*, 2006, **50**:147–67.

[24] Kemper, A. R., *et al*. (2005) Material properties of human rib cortical bone from dynamic tension coupon testing. *Stapp Car Crash Journal*, **49**: pp. 199–230.

[25] Kemper, A. R., *et al*. (2007) The biomechanics of human ribs: material and structural properties from dynamic tension and bending tests. *Stapp Car Crash Journal*, **51**(October): pp. 235–73.

[26] Schoell, S. L., *et al.* (2015) Development and Validation of an Older Occupant Finite Element Model of a Mid-Sized Male for Investigation of Age-related Injury Risk. *Stapp Car Crash Journal*, **59**(April 2016): pp. 359–83.

[27] Davis, M. L., Koya, B., Schap, J. M., Gayzik, F. S. (2016) Development and Full Body Validation of a 5th Percentile Female Finite Element Model. *Stapp Car Crash Journal*, **60**(November): pp. 509–44.

[28] Agnew, A. M., Stout, S. D. (2012) Brief communication: Reevaluating osteoporosis in human ribs: The role of intracortical porosity. *American Journal of Physical Anthropology*, **148**(3): pp. 462–6.

[29] McCalden, R. W., McGeough, J. A., Barker, M. B., Court-Brown, C. M. (1993) Age-Related Changes in the Tensile Properties of Cortical Bone. *The Journal of Bone and Joint Surgery*, **75–A**(8): pp. 1193–205.

VIII. APPENDIX

A. Modifications to the THUMS v3 model

Body Part		Modification
Chest	**Ribs**	**Geometry and mesh modified** "Shi, X., *et al*. (2014) A statistical human rib cage geometry model accounting for variations by age, sex, stature and body mass index. *Journal of Biomechanics,* **47**(10): pp. 2277–85." **Cortical bone thickness modified** "Choi, H-Y, Kwak, D-S (2011) Morphologic Characteristics of Korean Elderly Rib. *Journal of Automotive Safety and Energy*, ;**2**." **Cortical bone properties modified** "Kemper, A. R., *et. al*. (2005) Material properties of human rib cortical bone from dynamic tension coupon testing. *Stapp Car Crash Journal,* **49**: pp. 199–230. "Kemper, A. R., et al. (2007) The biomechanics of human ribs: material and structural properties from dynamic tension and bending tests. *Stapp Car Crash Journal,* **51**: pp. 235–73."
	Sternum	**Geometry and mesh modified** 50th percentile male sternum "Weaver, A. A., Schoell, S. L., Nguyen, C. M., Lynch, S. K., Stitzel, J. D. (2014) Morphometric analysis of variation in the sternum with sex and age. *Journal of Morphology,* **275**(11): pp. 1284–99."
Lumbar Spine	**Vertebra**	**Remeshed** Contact between vertebra and intervertebral disk added Intervertebral ligaments modified – both geometry and properties "Afwerki, H. (2016) Biofidelity Evaluation of Thoracolumbar Spine Model in THUMS. Master's Thesis in Biomedical Engineering, Chalmers University of Technology."
Head		**New Head Model** "Kleiven, S. (2007) Predictors for Traumatic Brain Injuries Evaluated through Accident Reconstructions. *51st Stapp Car Crash Journal,:* pp. 81–114."

B. Sled test modelling validation with matched test and simulations

The sled test modelling method used recorded accelerations from the corresponding tests to drive the model sled and ASIS. Similarly, the airbag model pressure was prescribed to the pressures recorded from the corresponding test. To validate the sled modelling methodology, matched test and simulation was conducted with a SID-IIs dummy and a LS-Dyna dummy model (SID-IIs SBL-D V3.3.2, Humanetics Innovative Solutions, Inc).

Fig. B.1 shows the accelerations measured in the test, which were used to drive the sled model. The airbag pressures obtained in the test and applied in the model can be seen in Fig. B.2.

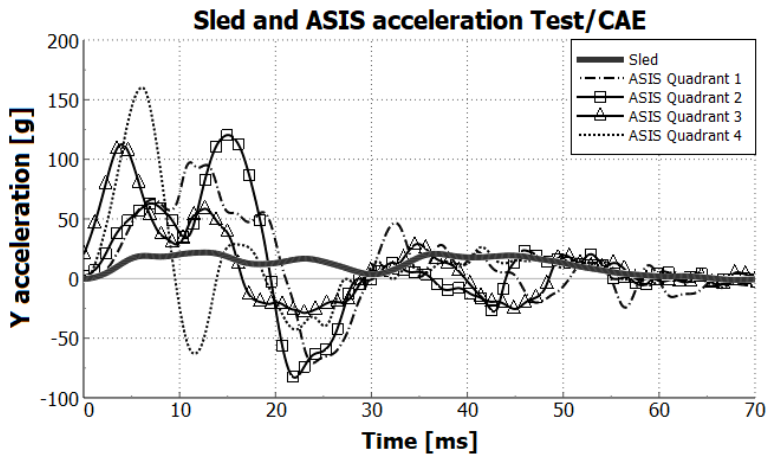

Fig. B.1. The accelerations measured in the sled test used to drive the sled model and ASIS in the validation simulation (CAE).

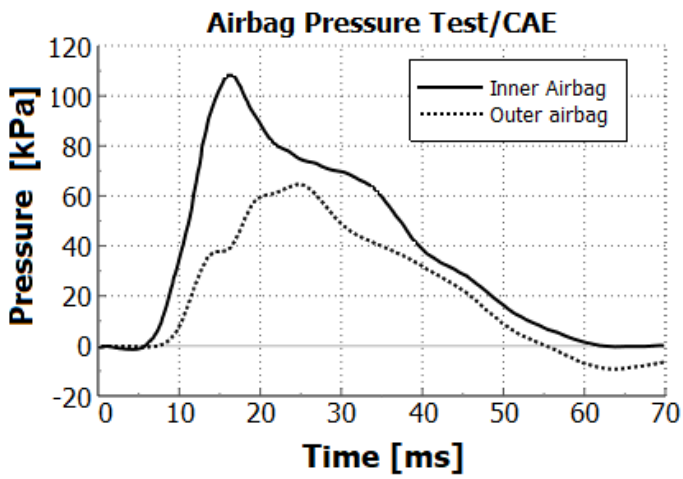

Fig. B.2. Airbag pressures measured in the test and applied to the airbag model in the sled test simulation.

SID-IIs measured accelerations from test and simulation (CAE) can be seen in Fig. B.3, and rib deflection from test and simulation in Fig. B.4.

Shoulder and Top thoracic rib deflections and T12 lateral acceleration overshot the test results in the sled test simulation model at 50 ms. If this was due to SID-IIs CAE model to SID-IIs hardware correlation issues or due to the sled modelling technique is not clear. However, the general shape of deflections were predicted by the sled modelling method, and the results were accurate at least up to the AIS3 thoracic injury timing of both PMHS tests (39 ms in 1701, 21 ms in 1702, TABLE I).

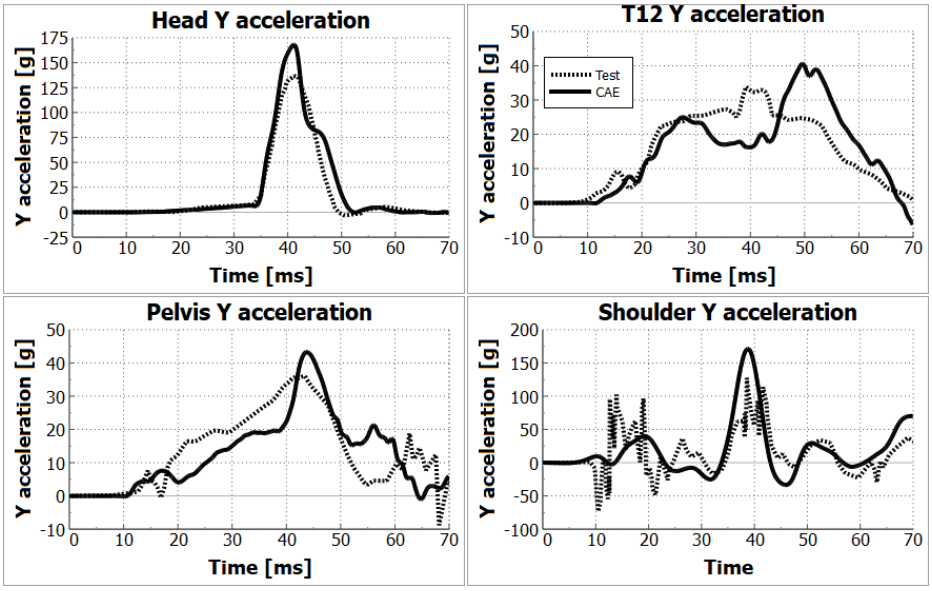

Fig. B.3. SID-IIs Lateral accelerations measured in test (dashed curves) and simulation (solid curves).

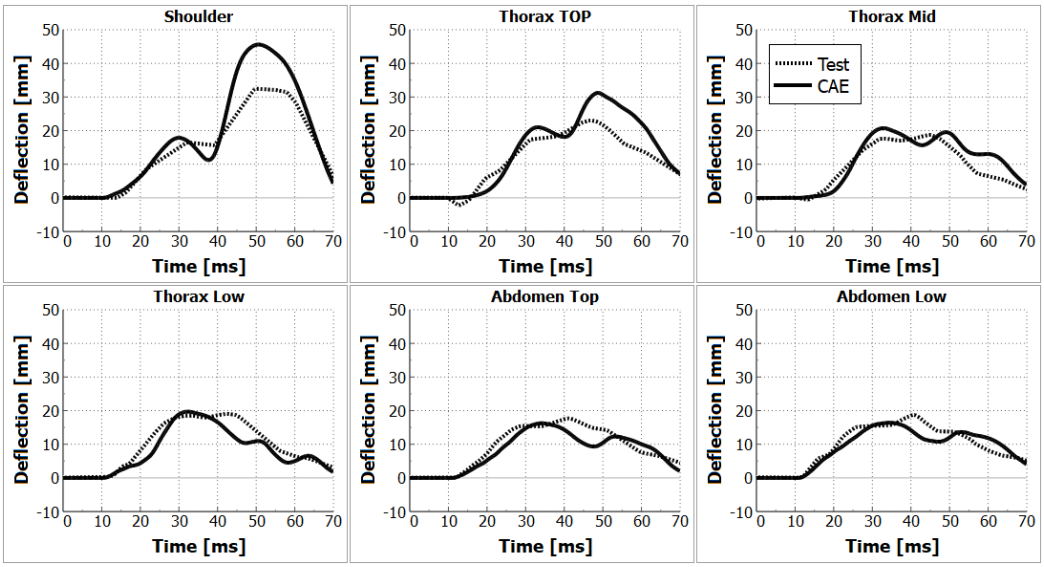

Fig. B.4. SID-IIs rib deflections measured in test (dashed curves) and simulation (solid curves).

C. Shoulder and External torso shape personalization morphing

For the humerus, scapula and clavicle (shoulder), morphing tools in the software Ansa v.18.1.1 (BETA CAE systems SA, Thessaloniki, Greece) were used to align the parametrically morphed HBM bone surface to the surface of the respective segmented bones, such that the personalized HBMs would have the approximate bony shoulder geometry as the respective subject (Fig. C.1, Fig. C.2). The nodes on the aligned HBM bone surfaces were used as target landmarks, and the corresponding nodes on the parametrically morphed HBMs were used as source landmarks. The RBF morphing landmark selection was only done for the left side, and the selected landmarks were reflected to the right side. The bones and surrounding elements were morphed while keeping the personalized ribcage fixed.

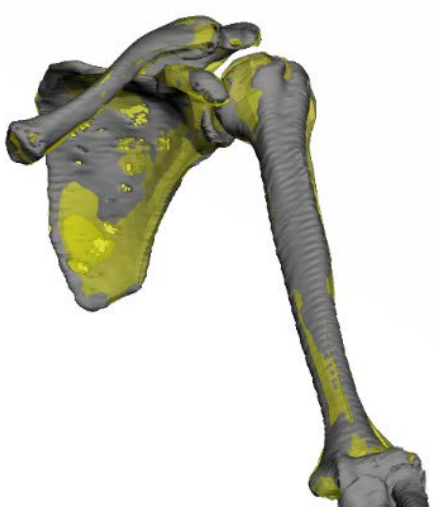

Fig. C.1. Test 1701 Segmented left-side clavicle, scapula and humerus (gray) and aligned HBM mesh (yellow) used for creating landmarks for personalization morphing.

Fig. C.2. Test 1702 Segmented left-side clavicle, scapula and humerus (gray) and aligned HBM mesh (yellow) used for creating landmarks for personalization morphing.

For the external torso shape morphing, target landmarks were obtained by fitting a spline curve to the plots of computed chestband profiles at time zero (see e.g. black curves in Fig. 8). The created splines were then positioned at the axilla or xiphoid level and aligned with spine and sternum on the HBMs. On these splines, 128 points were generated on each with equal distance, which corresponds to the number of nodes on the circumference of the model chestbands. The 128 points were then copied 15 mm up and down along the torso to create the 3*128 target landmarks for middle, top and bottom edges of the 30 mm-wide model chestbands. Source landmarks were chosen as the nodes from the corresponding top, middle and bottom edges of the parametrically morphed model chestbands. The external torso surface was then morphed while keeping personalized ribcage and shoulders fixed.

D. Chestband deformation contours

The chestband contours from test and Baseline, Parametric and Personalized HBM simulations used for calculating chest band deflection measurements are shown in Fig. D.1 for test 1701 and Fig. D.2 for test 1702.

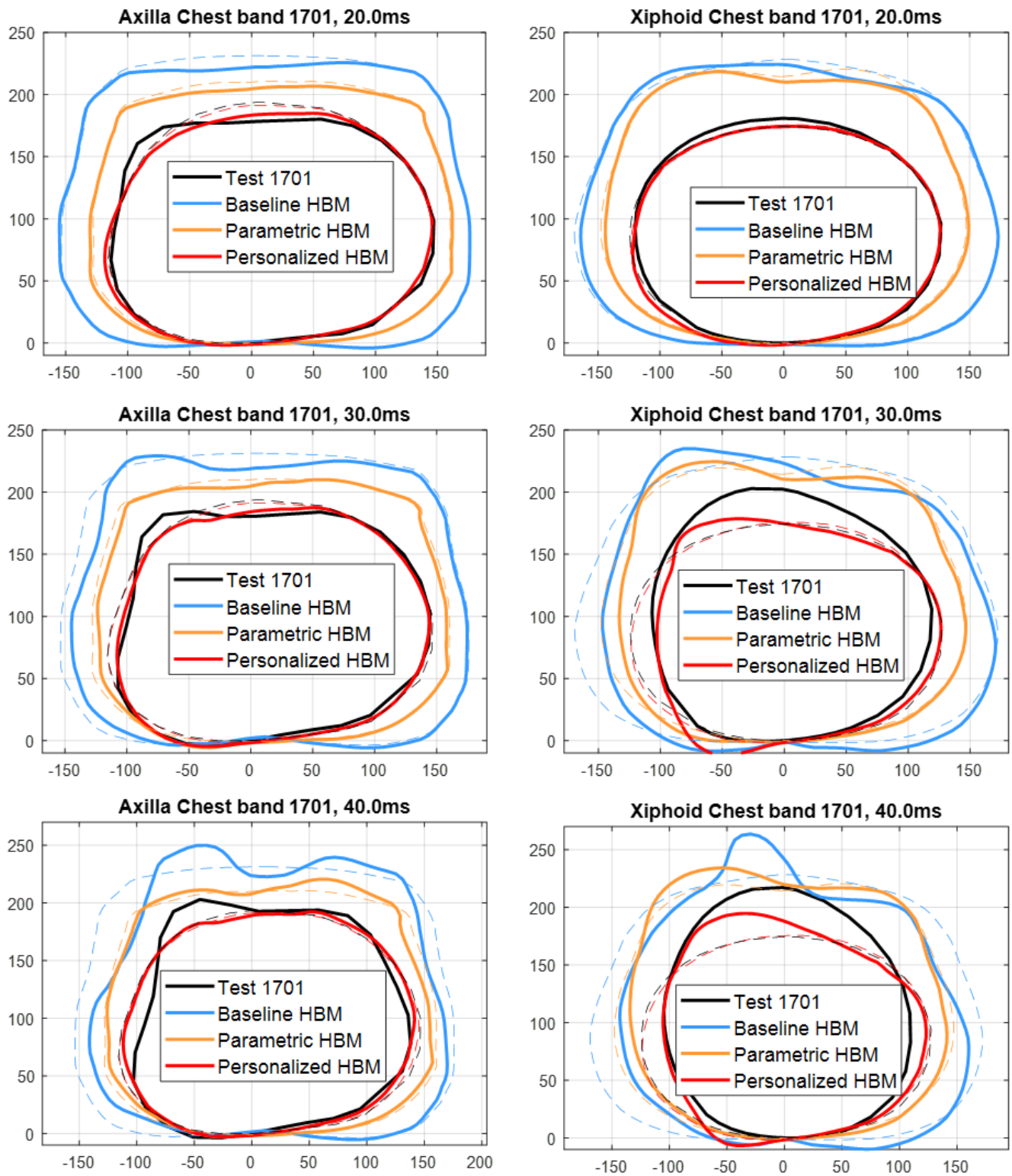

Fig. D.1. Test 1701 chestband deformation contours at 20 ms, 30 ms and 40 ms. *Left* column is Axilla level chest band and *Right* column is Xiphoid level chestband.

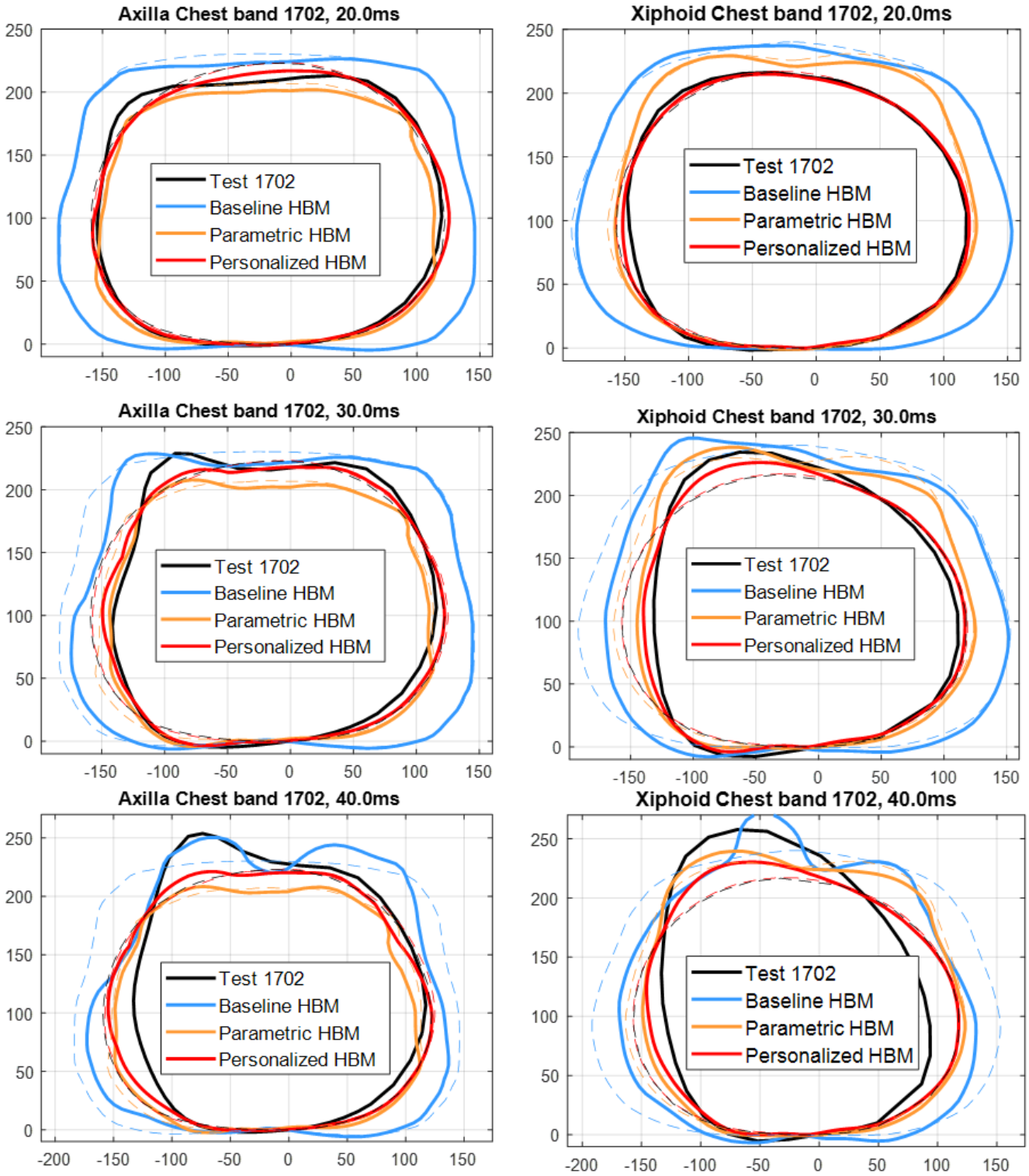

Fig. D.2 Test 1702 chestband deformation contours at 20 ms, 30 ms and 40 ms. *Left* column is Axilla level chest band and *Right* column is Xiphoid level chestband.

E. Rib strain measurements from test and simulations

In test 1701 strain gauges were located on the lateral aspect of the left-side ribs L4-L10, and posterior on ribs L5-L9. Test 1701 left rib strain measurements are shown in Fig. E.1.

Test 1702 had strain gauges closer to the anterior end of ribs L2-L10 and posterior on ribs L4-L9. Test 1702 rib strain measurements, ribs L2-L7 are shown in Fig. E.2, and ribs L8-L10 in Fig. E.3.

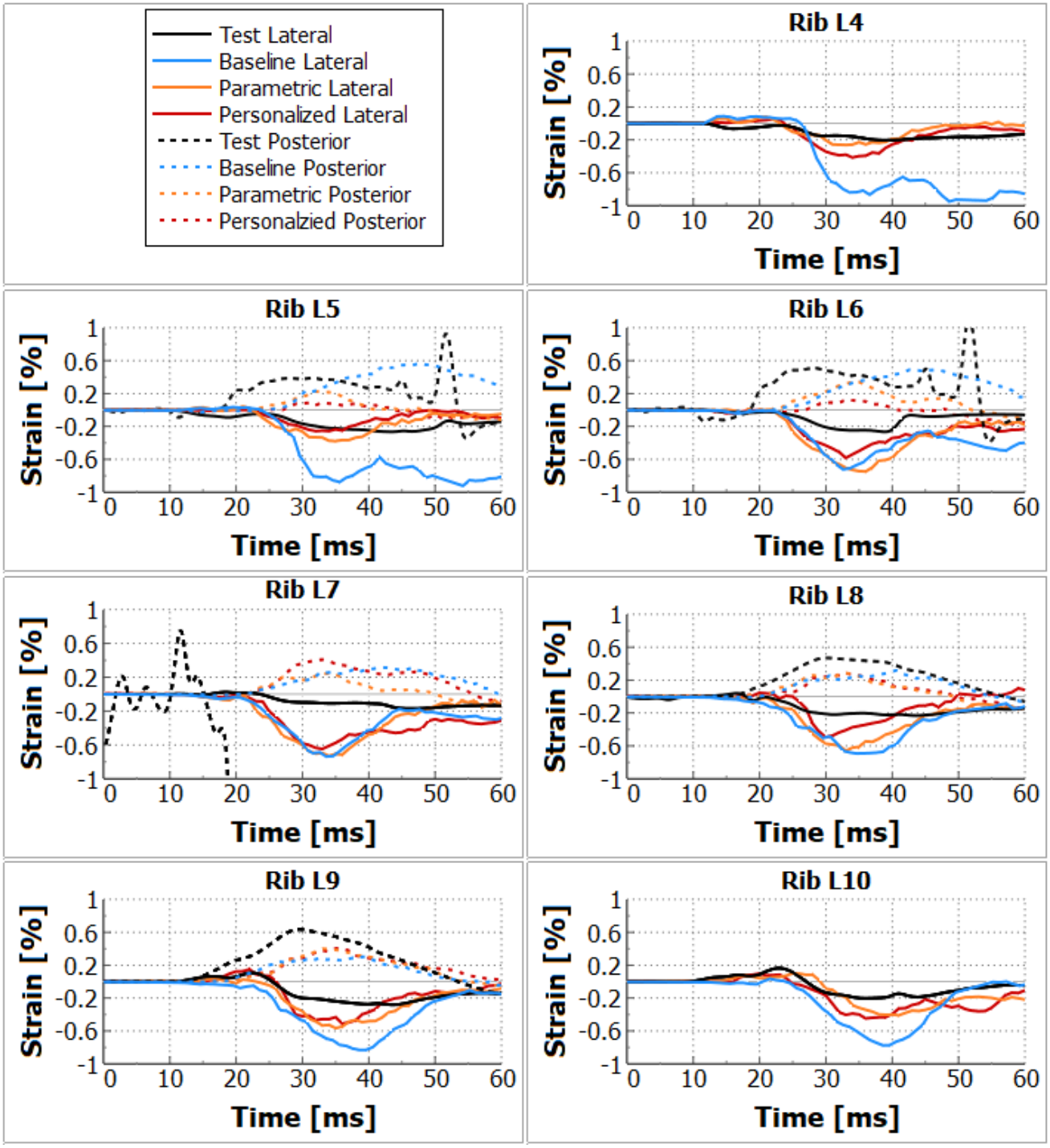

Fig. E.1. Test 1701 rib strain measurements. Lateral strain gauges are solid curves, posterior gauges dashed curves. Test (black), Baseline HBM (blue), Parametric HBM (orange), Personalized HBM (red).

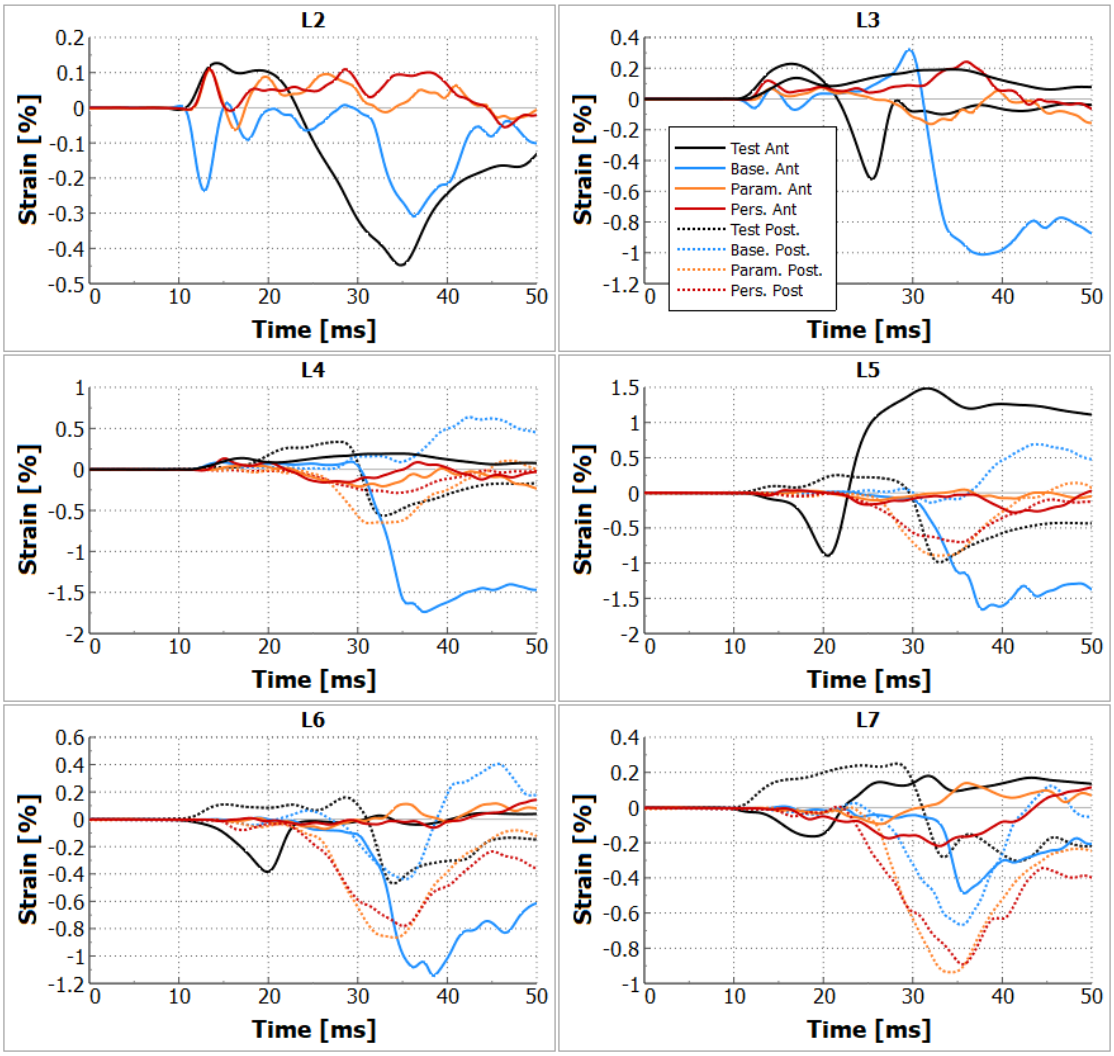

Fig. E.2. Test 1702 left rib strain measurements, L2-L7. Anterior strain gauges are solid curves, posterior gauges dashed curves. Test (black), Baseline HBM (blue), Parametric HBM (orange), Personalized HBM (red).

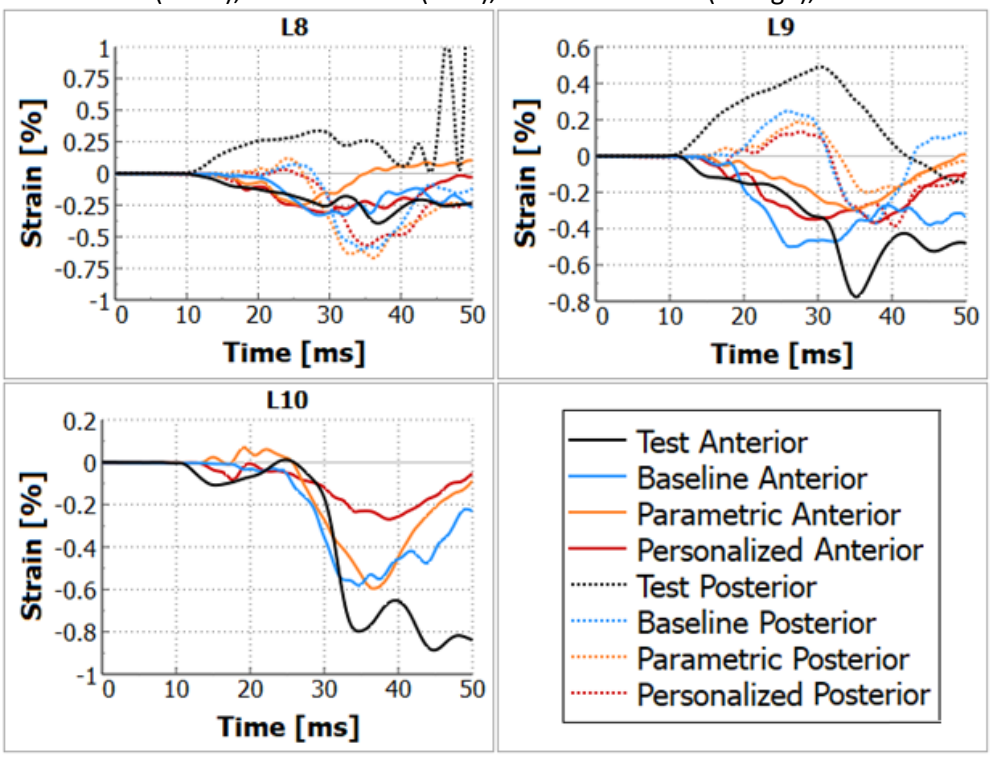

Fig. E.3. Test 1702 left rib strain measurements, L8-L10. Lateral strain gauges are solid curves, posterior gauges dashed curves. Test (black), Baseline HBM (blue), Parametric HBM (orange), Personalized HBM (red).

F. Shoulder-belt forces test and simulation

Shoulder-belt force magnitudes during test and simulation are displayed in Fig. F.1 for test 1701 and Fig. F.2 for test 1702.

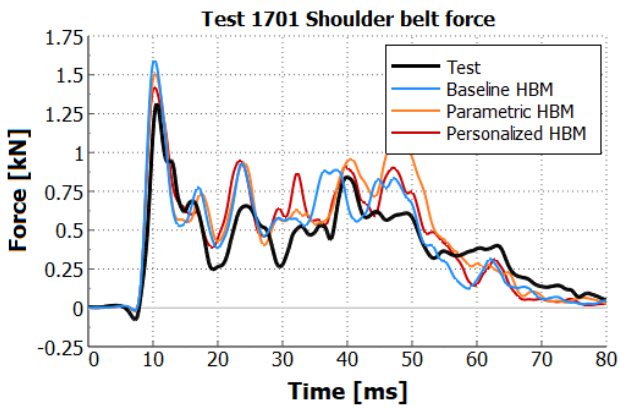

Fig. F.1. Shoulder-belt force from test 1701 and simulations. Test (black), Baseline HBM (blue), Parametric HBM (orange), Personalized HBM (red).

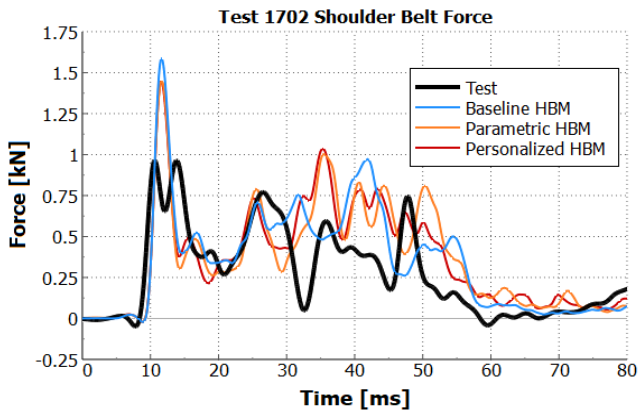

Fig. F.2. Shoulder-belt force from test 1702 and simulations. Test (black), Baseline HBM (blue), Parametric HBM (orange), Personalized HBM (red).

G. Comparison of flesh model viscoelastic response THUMS v3 torso vs modified Östh *et al.* neck flesh

The Östh *et al.* [22] flesh modelling (*MAT_OGDEN_RUBBER for solids and *MAT_ELASTIC for skin) was modified in the 1 mm skin membrane shell element material response. Originally a linear elastic material of 1 MPa Young's modulus was used by Östh when validating the head-neck model for low-speed rear impact (ΔV=1.3-2.6 m/s). For higher severity impacts a non-linear stress strain response that gradually increases the stiffness up to the 22 MPa of the original THUMS v3 skin material was implemented (Fig. G.1) by a unidirectional LS-Dyna *MAT_FABRIC constitutive material model with compressive stress elimination.

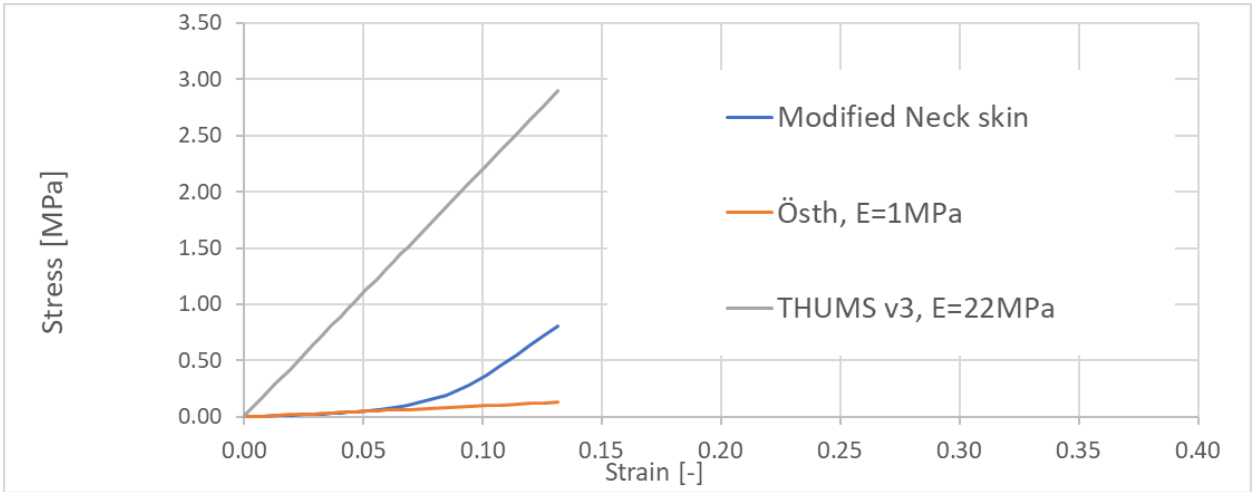

Fig. G.1. Stress vs strain response for three skin models: THUMS v3 (gray), Östh (orange), Modified Östh (blue).

To quantify the difference in viscoelastic material response between the THUMS v3 original torso flesh modelling (*MAT_VISCOELASTIC for solids and *MAT_ELASTIC for skin) and the modified Östh *et al.* flesh modelling, two simulations series were performed.

In the first, a cylindrical sample of radius 50 mm and height 18 mm, approximately 3 mm mesh was impacted by a half-spherical rigid impactor with radius 15 mm with varying constant velocities (Fig. G.2). The circumference of the sample was constrained. The top and bottom surface was covered with the respective skin elements from the two modelling methods and the volume of the sample used the respective soft tissue material modelling.

Force versus sample top surface centre deflection was plotted for impactor velocities of 0.1 metres per second, 1 mps and 10 mps (Fig. G.3). In all impact velocities the THUMS v3 flesh modelling (Old) required a larger force for the same deflection.

Fig. G.2. The rigid impactor striking the flesh modelling sample with constant velocity.

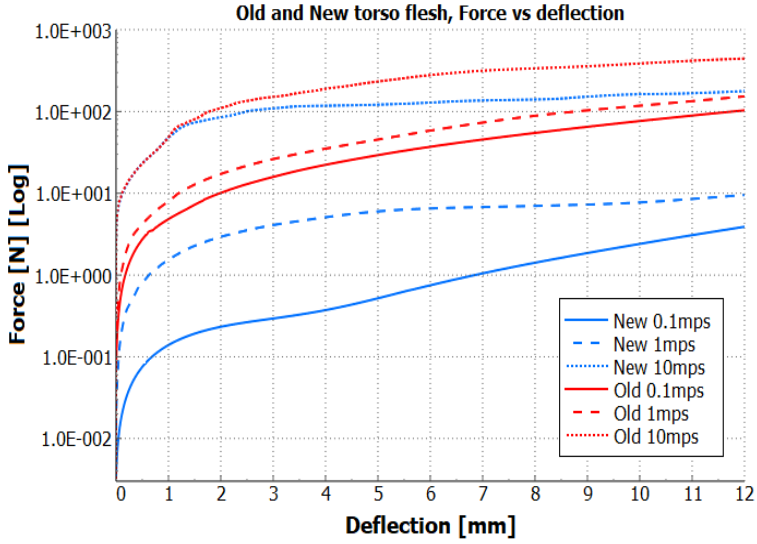

Fig. G.3. Force versus sample deflection for the two flesh models. Logarithmic scale. New (blue curves) refers to the modified (Östh *et al.*) flesh modelling. Old (red curves) refers to the original THUMS v3 flesh modelling.

In the second simulation series, a cylindrical sample with 10 mm radius and 25 mm height was modelled with approximately 0.6 mm hexahedral elements of the corresponding flesh material models. The solid elements were coated with the respective skin shell elements. The bottom surface of the sample was kept fixed and the top surface was rotated with constant rotational velocity of 0.1 rad/ms and 1 rad/ms. Moment versus rotation angle was plotted (Fig. G.5). For both rotational velocities the modified Östh (New) provided a softer response than the THUMS v3 (Old) flesh modelling.

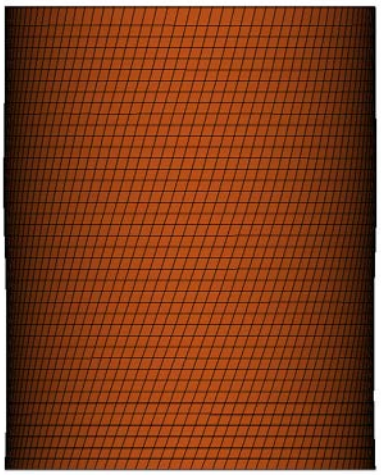

Fig. G.4. The cylindrical flesh model sample being twisted under constant velocity.

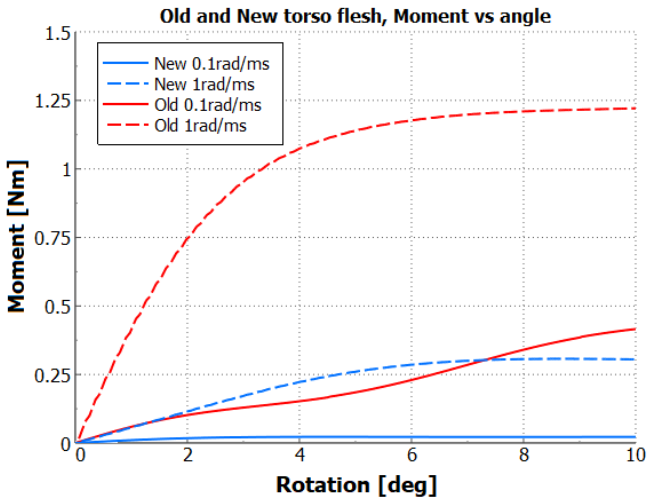

Fig. G.5. Moment versus angle response for the two flesh models. New (blue curves) refers to the modified Östh *et al.* flesh modelling. Old (red curves) refers to the original THUMS v3 flesh modelling.